Ethacridine inhibits SARS-CoV-2 by inactivating viral particles in cellular models

Xiaoquan Li[1, 2#], Peter Lidsky[3#], Yinghong Xiao[3#], Chien-Ting Wu[4], Miguel Garcia-Knight[3], Junjiao Yang[1, 2], Tsuguhisa Nakayama[5], Jayakar V. Nayak[5], Peter K. Jackson[4], Raul Andino[3, *], Xiaokun Shu[1, 2, *]

Affiliations:

[1]Department of Pharmaceutical Chemistry, University of California, San Francisco, San Francisco, California, USA.

[2]Cardiovascular Research Institute, University of California, San Francisco, San Francisco, California, USA

[3]Department of Microbiology and Immunology, University of California, San Francisco, San Francisco, California, USA.

[4]Department of Baxter Laboratory for Stem Cell Biology, Department of Microbiology & Immunology, Stanford University, California, USA

[5]Department of Otolaryngology–Head and Neck Surgery, Stanford University, Stanford, California, USA

[#]These authors contributed to the work equally.

[*]Correspondence to: Raul Andino (email: raul.andino@ucsf.edu); Xiaokun Shu (email: xiaokun.shu@ucsf.edu)

Abstract

More than a million people have now died from COVID-19, because of infection with the SARS-CoV-2 coronavirus. Currently, the FDA has approved remdesivir, an inhibitor of SARS-CoV-2 replication, to treat COVID-19, though very recent data from WHO showed little if any COVID19 protective effect. Here we report that ethacridine, a safe and potent antiseptic use in humans, effectively inhibits SARS-CoV-2, at very low concentrations ($EC_{50} \sim 0.08\ \mu M$). Ethacridine was identified through a high-throughput screening of an FDA-approved drug library in living cells using a fluorescent assay. Interestingly, the main mode of action of ethacridine is to inactivate virus particles, preventing binding to the host cells. Thus, our work has identified a potent drug with a distinct mode of action against SARS-CoV-2.

Introduction

The worldwide outbreak of the respiratory disease COVID-19 is caused by the coronavirus SARS-CoV-2 (severe acute respiratory syndrome coronavirus 2). SARS-CoV-2 is an RNA betacoronavirus of the family *Coronaviridae*. It contains a single-stranded positive-sense RNA genome encapsulated within a membrane envelope [1-4]. Its genomic RNA is approximately 30kb with a 5′-cap structure and 3′-poly-A tail [1]. The genome of SARS-CoV-2 can be split into two main regions that contain as many as 14 open reading frames (ORFs) [5].

The first region, containing the first ORF (ORF1a/b), is about two-thirds of the genome length. After coronavirus attachment and entry into the host cell, the viral genomic RNA is released. The first region of the genomic RNA is used as a template to directly translate two polyproteins: pp1a and pp1ab. The pp1a polyprotein is translated from ORF1a. The pp1ab polyprotein comes from a -1 ribosomal frameshift between ORF1a and ORF1b. The two overlapping polyproteins are processed by a papain-like protease (PLpro) and a 3-chymotrypsin-like protease (3CLpro), which is also referred to as the main protease - Mpro. Both pp1a and pp1ab are mainly processed by Mpro, which digests the polyproteins at no less than 11 conserved sites, starting with the auto-proteolytic cleavage of this viral protease itself from pp1a and pp1ab. The functional polypeptides, 16 non-structural proteins (nsp1–16), are released from the polyproteins after extensive proteolytic processing. Nsp12 (i.e., RNA-dependent RNA polymerase (RdRp)), together with other nsps (e.g., nsp7 and nsp8), forms a multi-subunit replicase/transcriptase complex (RTC) that is associated with the virus-induced double-membrane vesicles [4,6,7]. The membrane-bound RTC synthesizes a full-length negative-strand RNA template that is used to make positive-strand viral genomic RNA.

The remaining one-third of the genomic RNA is used by the RTC to synthesize subgenomic RNAs (sgRNAs) that encode four conserved structural proteins (spike protein (S), envelope protein (E), membrane protein (M), and nucleocapsid protein (N)), and several accessory proteins. Eventually, the viral RNA-N complex and S, M, and E proteins are assembled in the ER-Golgi intermediate compartment (ERGIC) to form a mature virion that is then released via budding from the host cell. S protein is exposed on the surface of the virion and binds the virus receptor ACE2 on the host cell surface. Therefore, Mpro plays a central and critical role in the lifecycle of the coronavirus and is an attractive drug target [8-10], which also include other biological steps essential for viral replication and budding.

To identify drugs that inhibit the coronavirus, we redesigned green fluorescent protein (GFP) into an activity reporter of Mpro that becomes fluorescent only upon cleavage by the active Mpro. Using this assay, we screened a drug library in living cells and identified several drugs that inhibit Mpro activity. One highly effective drug, ethacridine, inhibits SARS-CoV-2 production by inactivating the viral particles.

RESULTS

Rational design of a fluorogenic Mpro activity reporter FlipGFP^{Mpro}

To develop an activity reporter of Mpro with a large dynamic range suitable for high-throughput screening (HTS), we applied the GFP-based protease reporter called FlipGFP

[11], which was designed by flipping one of the 11 beta-strands of a split GFP. Briefly, the split GFP contains two parts: one part contains beta-strands 10 and 11 (i.e., GFP10 and 11), and the other contains nine other beta-strands and the central alpha helix (i.e., GFP1–9). GFP10–11 contains the highly conserved Glu222 that is essential for catalyzing chromophore maturation. GFP1-9 contains the three amino acids that form the chromophore via cyclization, dehydration and oxidation [12]. GFP10-11 spontaneously binds GFP1-9 and catalyzes the chromophore maturation, leading to a GFP. To design an Mpro activity reporter, we "flipped" GFP10-11 using heterodimeric coiled coils (E5 and K5) so that the flipped GFP10-11 cannot bind GFP1-9 when Mpro is inactive, and thus, no or little fluorescence is detected (**Fig. 1a**). We incorporated an Mpro-specific cleavage sequence AVLQ↓SGFR (↓ denotes the cleavage site) between GFP11 and K5. In this way, when Mpro cleaves the proteolytic site, GFP11 flipped back, which allowed GFP10-11 to bind GFP1-9, resulting in bright fluorescence (**Fig. 1a**). We named this reporter FlipGFP^{Mpro}. To normalize the fluorescence, we added a red fluorescent protein mCherry in the construct via a "self-cleaving" 2A peptide[13] (**Fig. 1c**).

To determine if FlipGFP^{Mpro} reports on SARS-CoV-2's Mpro activity in living cells, we expressed the human ACE2, SARS-CoV2 receptor, in HEK293-FlipGFP^{Mpro} cells. Next, we infected the cells with SARS-CoV-2, and at 24 hours post-infection, cells were analyzed by immunofluorescence using antibodies directed against double-stranded RNA (dsRNA) and by the FlipGFP^{Mpro} signal. The green fluorescence of the sensor FlipGFP^{Mpro}, normalized by the co-expressed mCherry, was 63% greater in the infected cells than in non-infected cells (**Fig. 1d**). Infected cells also showed dsRNA fluorescence. In contrast, non-infected (mock) cells showed no dsRNA staining (**Fig. 1d**). These data, thus, demonstrate that FlipGFP^{Mpro} can report on SARS-CoV-2 Mpro activity in living cells.

Next, we established a system for screening Mpro inhibitors in living cells by exogenously expressing Mpro in HEK293. Specifically, we co-expressed wild-type Mpro or an inactive Mpro mutant in which the catalytic cysteine 145 is mutated to alanine. The green fluorescence of FlipGFP^{Mpro} was barely detected in the cells expressing the inactive Mpro/C145A mutant, whereas the red fluorescence of mCherry was observed (**Fig. 1e**, upper panels). On the other hand, strong green fluorescence was detected in the cells expressing Mpro with similar levels of mCherry fluorescence (**Fig. 1e**, lower panels). The green fluorescence of FlipGFP^{Mpro}, normalized to the red fluorescence of mCherry, revealed an ~60-fold dynamic range between inactive and active Mpro (**Fig. 1f**). Furthermore, based on these quantified data, we calculated a *Z'-factor*[14]

$$Z = 1 - \frac{(3\sigma_+ + 3\sigma_-)}{|\mu_+ - \mu_-|},$$

which is ~0.8 with Mpro and its inactive mutant as positive (+) and negative (-) controls, respectively (here σ is standard deviation, μ is mean). This suggests that the assay is robust for HTS.

The FlipGFP^{Mpro} sensor was not responsive to the TEV protease, and the FlipGFP-based TEV reporter (FlipGFP^{TEV}) was only activated by TEV but not by Mpro (**Fig. 1f**). Thus, FlipGFP^{Mpro} specifically detects Mpro activity with a large dynamic range. Therefore, our data show that we have established a robust HTS system for screening Mpro inhibitors at a BSL2 level with 60-fold fluorescence change and a robust z'-factor. Comparing the normalized FlipGFP^{Mpro} fluorescence in the SARS-CoV-2 infected cells (**Fig. 1d**) with that from the exogenously Mpro-expressing cells (**Fig. 1e, f**)

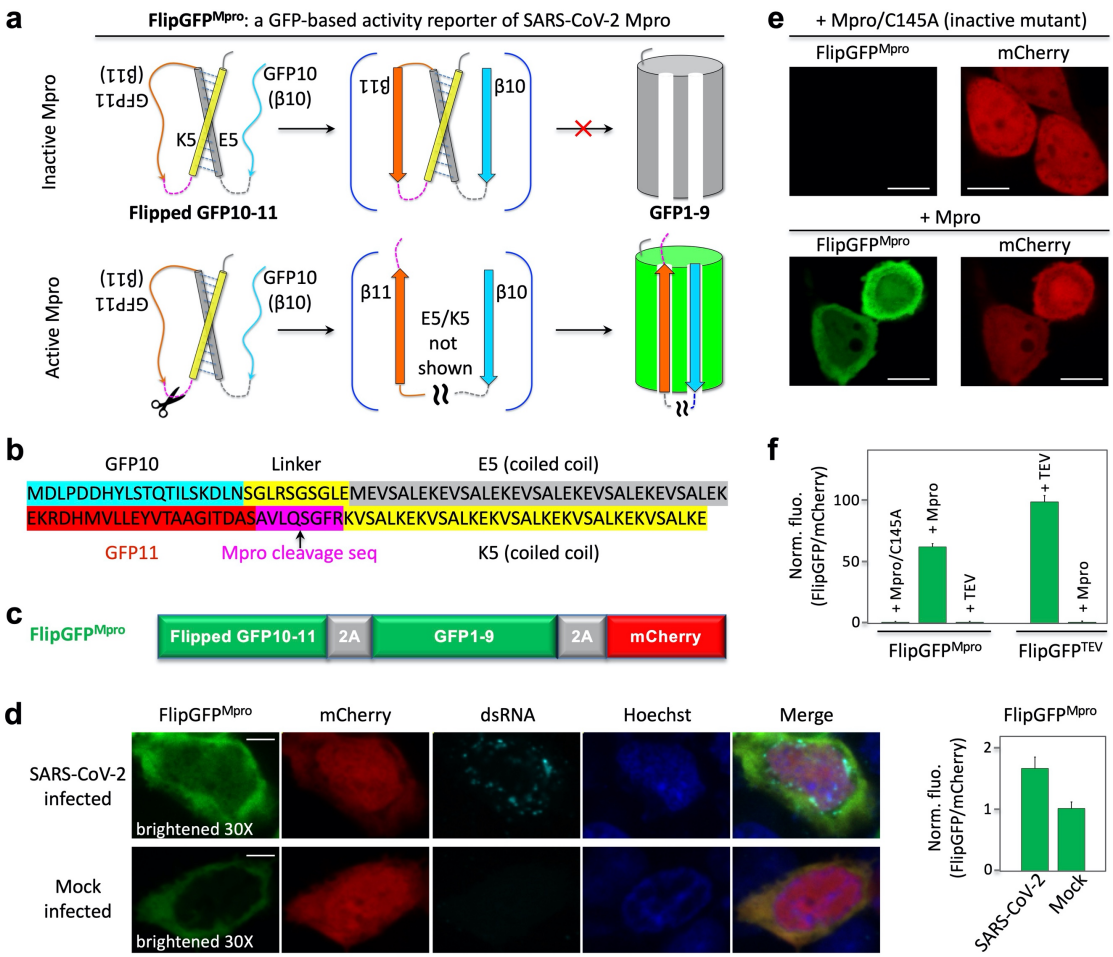

Fig. 1. Design and demonstration of a GFP-based activity reporter of SARS-CoV-2 main protease Mpro. (**a**) Schematic of the reporter. (**b**) Sequence of the flipped GFP10-11. (**c**) Construct of the reporter FlipGFP^{Mpro}. (**d**) Fluorescence images (left) and quantitative analysis (right) of SARS-CoV-2 or mock-infected HEK293T cells that co-expressed hACE2. The images in the FlipGFP channel were brightened 30-fold compared to those in (**e**). (**e**) Fluorescence images of HEK293T cells expressing FlipGFP^{Mpro} and mCherry, together with the inactive Mpro mutant C145A (upper panels) or wild type Mpro (lower panels). (**f**) Normalized FlipGFP fluorescence by mCherry. The ratio of FlipGFP/mCherry for the Mpro/C145A is normalized to 1. Data are mean $\pm$ SD (n = 5). FlipGFP^{TEV} is a TEV activity reporter containing TEV cleavage sequence in FlipGFP. Scale bar: 5 μm (**d**); 10 μm (**f**).

129 suggests that the active Mpro concentration in the cytoplasm of the coronavirus-infected
130 cells is ~100-fold lower than that of the HEK293 cells exogenously expressing Mpro
131 (under a EF1α promoter).
132
133 **HTS of drugs that inhibit Mpro activity in living cells**
134 Next, we conducted HTS of ~1600 FDA-approved drugs (20 μM final concentration, **Fig.**
135 **2a**). The reporter construct (FlipGFP^{Mpro} and mCherry) was transfected into HEK293
136 cells, followed by addition and incubation of the drugs. Levels of green fluorescence
137 normalized to red fluorescence were calculated. A volcano plot revealed ~120 drugs that
138 showed ≥ 50% reduction of Mpro activity with a p-value < 0.001 (**Fig. 2a**). To confirm
139 this result, we re-screened the identified ~120 drugs under similar conditions (Extended
140 Data Fig. 1). We further examined those top 15 drugs at a lower concentration (10 μM)
141 and found that 12 drugs showed ≥50% reduction of FlipGFP^{Mpro} fluorescence
142 (normalized by mCherry) at 10 μM concentration (**Fig. 2b**). We finally calculated an IC_{50}
143 for each of the 12 drugs. Six drugs were at 2 – 6 μM (**Fig. 2c**), and the rest were above 6
144 μM (Extended data Fig. 2).
145
146 **Antiviral activity of identified drugs**
147 We next investigated antiviral activity of selected drugs in Vero E6 cells. The monolayer
148 cells were pretreated with the drugs for 3 hours and cultivated in the presence of the
149 compounds at a concentration of 5 μM. After 16 hours of incubation, the culture media
150 samples were collected, and the amount of infectious particles were estimated by plaque
151 assay (**Fig. 3a, b** & Extended Data Fig. 3). Our data revealed that nine of the 12 drugs
152 showed significant antiviral activity at 5 μM. Strong inhibition was detected for
153 ethacridine with 5 – 6 logs reduction in viral titer, simeprevir ~4-log reduction, ABT-199
154 ~2-log reduction, hydroxyprogesterone ~1-log reduction, cinacalcet ~1-log reduction.
155 Two of the 12 drugs (ivermectin and verteporfin) were cytotoxic at 5–13 μM in Vero E6
156 cells and, thus, were excluded from the further analysis (Extended Data Fig. 4). As a
157 comparison, we tested the antiviral effect of a reported Mpro inhibitor, ebselen, which
158 showed ~2-log reduction in viral titer. And the RdRp inhibitor remdesivir showed ~4-log
159 reduction.
160 Next, we determined dose-response curves for top five selected drugs. First, our
161 data revealed that the EC_{50} of four drugs (simeprevir, cinacalcet, ABT-199 and
162 hydroxyprogesterone) was 1–3 μM (**Fig. 3c – g**), within a range similar to their IC_{50} in
163 inhibiting Mpro (**Fig. 2c**). This was consistent with the expectation that SARS-CoV-2
164 replication is inhibited by inhibiting Mpro activity. Indeed, as we were finalizing this
165 study, a preprint report showed that simeprevir inhibits Mpro activity and SARS-CoV-2
166 [15]. On the other hand, ethacridine showed outstanding antiviral activity (EC_{50} ~ 0.08 μM,
167 **Fig. 3e**), which is 40-fold lower (i.e. stronger) than its Mpro-inhibiting activity (IC_{50} ~
168 3.54 μM, **Fig. 2c**). This suggests that the superior antiviral activity of ethacridine is not
169 mainly accounted for by its Mpro-inhibiting activity. Lastly, for comparison, we also
170 determined the EC_{50} of remdesivir ~0.52 μM in a side-by-side manner (**Fig. 3h**), which
171 indicates that ethacridine is more potent than remdesivir.
172
173 **Ethacridine inhibits SARS-CoV-2 by inactivating viral particles**

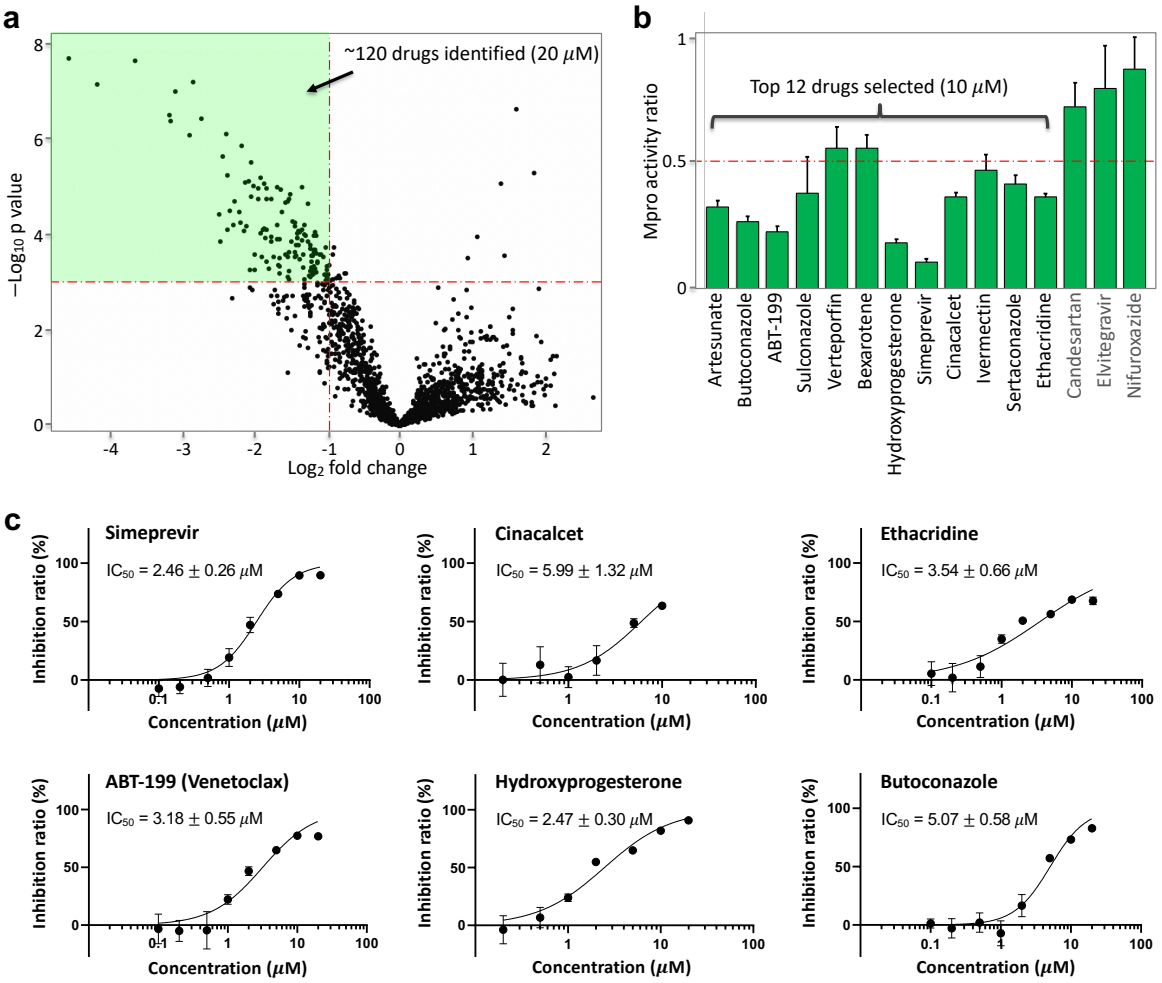

Fig. 2. High-throughput screening and drug identification using FlipGFP^{Mpro} in living cells. (**a**) Volcano plot of 1622 FDA-approved drugs (20 μM) in inhibiting Mpro. HEK293T cells were transfected with FlipGFP^{Mpro}, mCherry and Mpro. FlipGFP fluorescence was normalized to co-expressed mCherry. (**b**) Normalized ratio of Mpro activity in drug (10 μM) vs DMSO-incubated cells for the third-round validation. The Mpro activity was determined as FlipGFP fluorescence normalized to mCherry. The ratio of Mpro activity was calculated by normalizing Mpro activity with that of cells treated with DMSO. Data are mean $\pm$ SD (n = 5). The 15 drugs were identified from a second-round imaging of the 120 identified drugs (20 μM, Extended data Fig. 1). (c) Dose-response curve of top six drugs in inhibiting Mpro. Inhibition ratio was calculated as (1-(ratio of Mpro activity)) $\times$ 100%. IC_{50} was represented as mean $\pm$ SEM (n = 5). See Extended data Fig. 2 for the other six drugs.

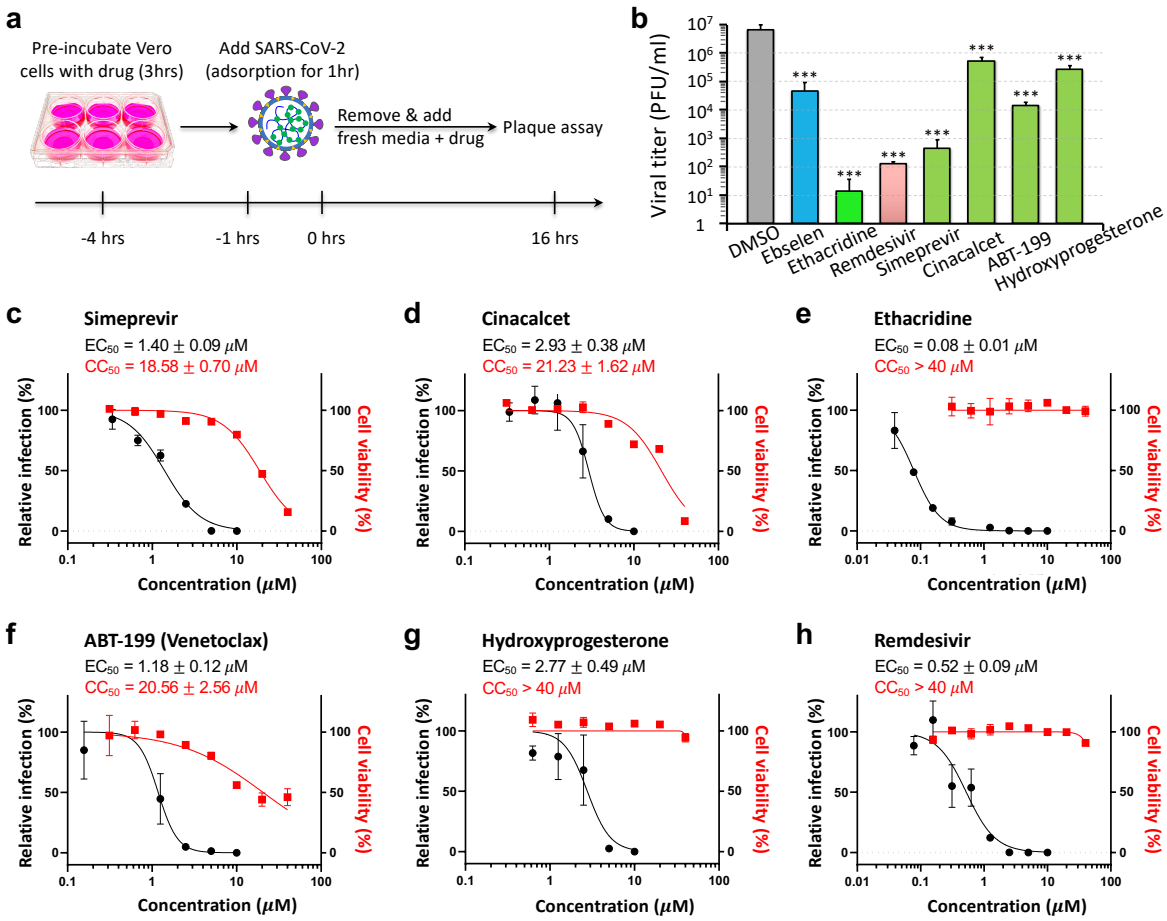

Fig. 3. Antiviral activities of the identified drugs against SARS-CoV-2. (**a**) Schematic showing the experimental design, see methods for details. (**b**) Quantitative analysis of viral titer from plaque assays on Vero E6 cells treated with each drug at 5 μM. Data are mean $\pm$ SEM (n = 3). *** $p < 0.001$. (**c–h**) Dose-response and cell-toxicity curve of each drug against SARS-CoV-2 by plaque assays. The percentage of relative infection was determined by the ratio of infection rate of SARS-CoV-2 treated with each drug divided by that of DMSO control. EC_{50} and CC_{50} are represented as mean $\pm$ SEM (n = 3).

174 To determine how ethacridine inhibits SARS-CoV-2, we tested infectivity of the virus
175 particles after ethacridine treatment using plaque assay, and we also measured viral RNA
176 levels using qRT-PCR. We examined antiviral effect of ethacridine on different stages of
177 the viral lifecycle of SARS-CoV-2, including before virus-cell binding, after cell entry,
178 and after budding. In particular, we pre-incubated SARS-CoV-2 particles with
179 ethacridine (5 μM) or DMSO for 1 hr. The mixture was then added to Vero E6 cells for
180 viral adsorption at a multiplicity of infection (MOI) at 0.5. Next, we removed the solution
181 and added fresh medium containing ethacridine (5 μM) or DMSO. Sixteen hours later,
182 we collected supernatant and conducted plaque assay with overlaid agar without
183 ethacridine or DMSO, measured viral titer of the supernatant. We also conducted qRT-
184 PCR and measured viral RNA levels in the supernatant and in the cells. By this way, we
185 developed three conditions (**Fig. 4a**): 1) Control (DMSO + DMSO): the virus and cells
186 were not exposed to the drug but DMSO; 2) The virus and cells were exposed to the drug
187 at all stages, including 1 hour before infection, during replication, and after viral budding
188 (i.e. Eth. + Eth.); 3) The virus and cells were exposed to the drug only after viral entry,
189 during replication, and after budding (i.e. DMSO + Eth.). Lastly, we used a fourth
190 condition (**Fig. 4b**): we conducted plaque assay right after pre-treatment of SARS-CoV-2
191 with ethacridine for 1 hr (i.e. Eth. [1 hr]), which determines antiviral activity of the drug
192 on the viral particles (equivalent to addition of the drug after viral budding).
193 When ethacridine was present all of the time (Eth. + Eth.), viral titers were
194 reduced 3 – 4 logs, compared with the control (DMSO + DMSO) (**Fig. 4a**, lower left
195 panel). When ethacridine was added to the Vero cells after viral entry (DMSO + Eth.),
196 similar level of reduction in infectivity (3 – 4 logs reduction in viral titer) was observed
197 (**Fig. 4a**). Interestingly, when SARS-CoV2 was pre-incubated with ethacridine for 1 hr
198 (Eth. [1 hr]) and followed by plaque assay without drug, we also observed 3 – 4 logs
199 reduction in infectivity (**Fig. 4b**). This result suggests that the drug inactivates SARS-
200 CoV2 particles infectivity. Because of similar-level reduction in infectivity in all of the
201 three conditions, our data strongly suggests that ethacridine inhibits SARS-CoV-2 by
202 mainly inactivating viral particles.
203 We next examined viral RNA accumulation in infected cells. qRT-PCR
204 measurement revealed no change of viral RNA (vRNA) levels when the drug was added
205 after viral binding and cell entry (DMSO + Eth.) in both the supernatant and the cells
206 (**Fig. 4a**, lower middle and right panels), compared with the control (DMSO + DMSO).
207 This indicates that the drug has no effect on vRNA replication. In contrast, if ethacridine
208 is present all of the time (i.e. Eth. + Eth.), we observed a reduction of 4 – 5 folds in
209 vRNA accumulation (**Fig. 4a**, lower middle and right panels). Because plaque assay-
210 based measurement of the same conditioned sample (Eth. + Eth.) showed 2400-fold
211 reduction in viral titer, the effect of ethacridine on viral replication (4 – 5 folds reduction)
212 is about 500-fold smaller than its effect on viral infectivity. This further supports that
213 ethacridine inhibits SARS-CoV-2 by inactivating the viral particles. The 4 – 5 folds
214 reduction of vRNA copies is likely due to partial inactivation of virus particles during
215 preincubation and thus a reduced number of infected cells (see below). Therefore, our
216 data suggests that ethacridine inhibits SARS-CoV-2 by mainly inactivating viral
217 particles, including those before infection, as well as new viruses after budding, with no
218 or little effect on vRNA replication (**Fig. 4c**).

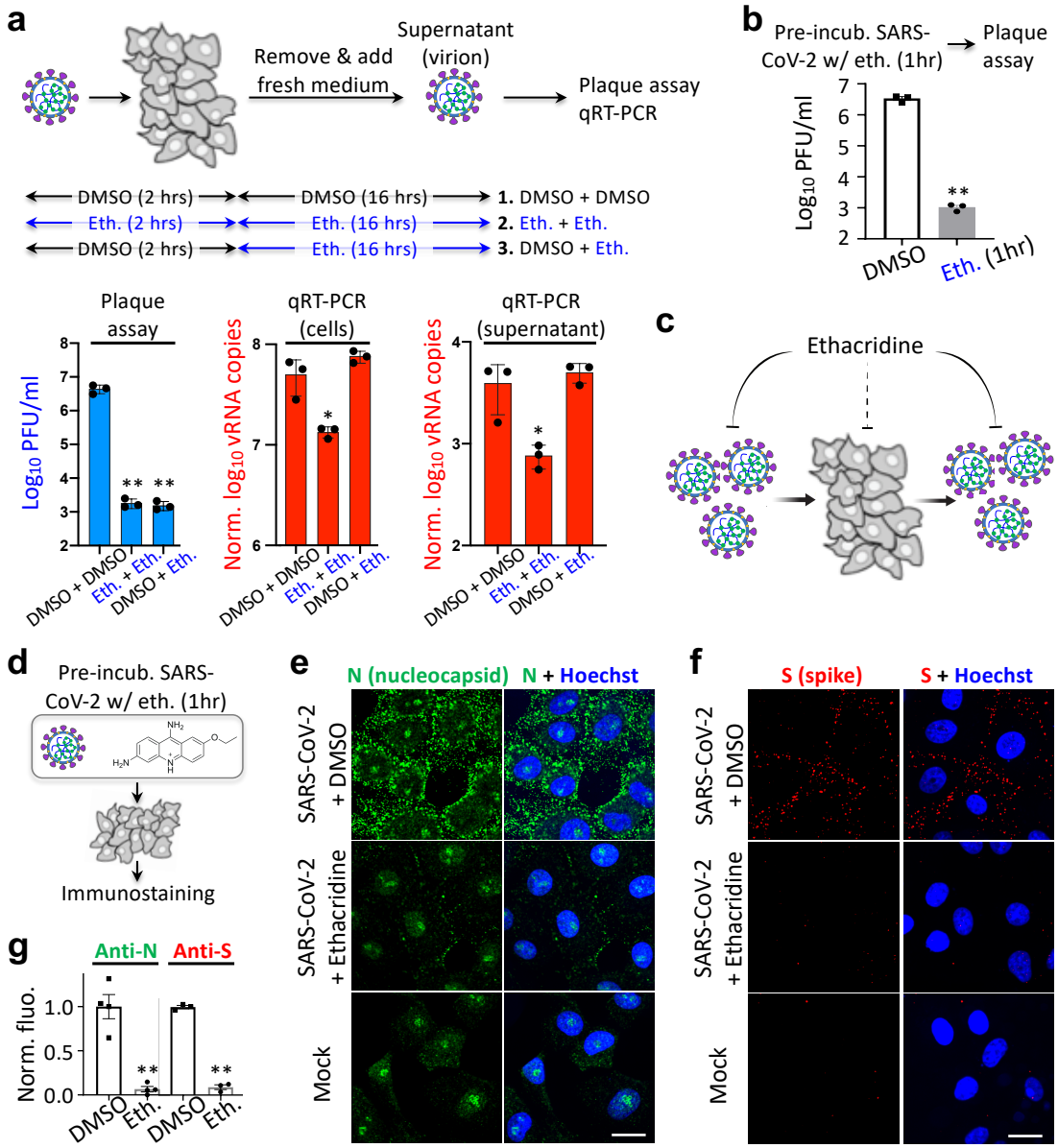

Fig. 4. Ethacridine bocks SARS-CoV-2 by inactivating viral particles.
(**a**) Upper panel: schematic showing the experimental design for plaque assay and qRT-PCR. The virus was pre-incubated with ethacridine or DMSO for 1 hr. The mixture was added to Vero cells for adsorption at 4°C for 1 hr. Details can be found in the text. Lower panel: quantitative analysis of viral titer from plaque assay (left), and viral RNA (vRNA) copies by qRT-PCR in Vero cells (middle) and supernatant (right). (**b**) Quantitative analysis of viral titer by plaque assay. (**c**) Proposed mode of action of ethacridine by mainly inactivating viral particles of the coronavirus with no or little effect on viral RNA replication. (**d**) Schematic showing the experimental design for immunostaining. (**e**, **f**) Representative images of immunostaining against nucleocapsid protein (N) and spike (S) in Vero E6 cells after infection with the virus that was pre-treated with ethacridine (5 μM) or DMSO (control), or no infection (mock). (**g**) Quantitative analysis of the immunofluorescence. Data are mean $\pm$ SEM (n = 3 or 4 biological replicas). **: p value < 0.01. *: p value < 0.05. Scale bar, 20 μm.

To further investigate the mechanism of ethacridine-based inactivation of the viral particles, we conducted immunostaining and fluorescence imaging to determine whether the ethacridine-treated SARS-CoV-2 can bind to and enter the cells. We treated SARS-CoV-2 with ethacridine (5 μM) or DMSO for 1 hour. Then the virus was added to cells for adsorption (37°C, 1 hour) at a MOI = 100. Cells were then quickly washed and fixed with 4% PFA (**Fig. 4d**). Immunostaining with antibodies against the nucleocapsid protein (N) of SARS-CoV-2 showed strong anti-N fluorescence on the plasma membrane of the cells infected with virus+DMSO mixture, but little anti-N fluorescence in cells treated with virus+ethacridine mixture (**Fig. 4e**). Immunostaining against Spike (S) of SARS-CoV-2 also revealed fluorescence signals on control cells, but little fluorescence on cells infected with the virus+ethacridine mixture (**Fig. 4f**). Quantification of fluorescence revealed that ethacridine treatment led to a significant reduction of the anti-N and anti-S fluorescence (**Fig. 4g**). These results indicate that ethacridine-treated SARS-CoV-2 cannot bind cells to initiate infection.

We also tested the dependency of the viral-inactivation effect of ethacridine on dose, incubation time and incubation temperature with a plaque assay. For the conditions tested, the viral-inactivation effect showed dose-dependency but was comparable to a 1- or 2-hour incubation at room temperature or 37°C (Extended data Fig. 5).

Further validation in human cells

We further evaluated the anti-viral effect of ethacridine in human cells, including a human lung epithelial A549 cell line stably expressing human ACE2 ($A549^{ACE2}$) and human primary nasal epithelial (HNE) cells to ensure that the antiviral effect is not restricted to the Vero E6 cells. A plaque assay in $A549^{ACE2}$ cells revealed that ethacridine-treated virus showed a dramatic decrease in infectivity (Extended data Fig. 6), indicating that the inhibitory effect of ethacridine is cell-type independent. To further support this and validate the antiviral effects, primary HNE cells were infected with ethacridine-treated virus and incubated with the media containing 5 μM ethacridine for 48 hours (**Fig. 5a**). Immunostaining using anti-N and anti-S antibodies in HNE cells showed that, in the presence of ethacridine, the proportion of infected cells was dramatically decreased (**Fig. 5b, c**), suggesting that ethacridine is also anti-viral in HNE primary cells. Thus, ethacridine is effective in a cell culture model of primary nasal epithelial cells at the air-liquid interface.

DISCUSSION

Several small molecule-based inhibitors have been identified that inhibit major targets involved in the viral lifecycle of SARS-CoV-2, including the main protease Mpro and the SARS-CoV-2 replicase RdRp. For example, α-ketoamide inhibitors of Mpro and the FDA-approved drug ebselen have been reported to inhibit Mpro activity with EC50 at 0.53 and 4.67 μM, respectively [8-10]. The replicase RdRp inhibitor, remdesivir, has been designed and very recently approved by FDA to treat severe COVID-19 patients [6,16]. However, very recent data from WHO showed no or little effect on hospital COVID-19 patients, including overall mortality, initiation of ventilation and duration of hospital stay [17]. Thus, therapeutic efficacy of remdesivir is far from satisfactory, and new therapies are urgently needed.

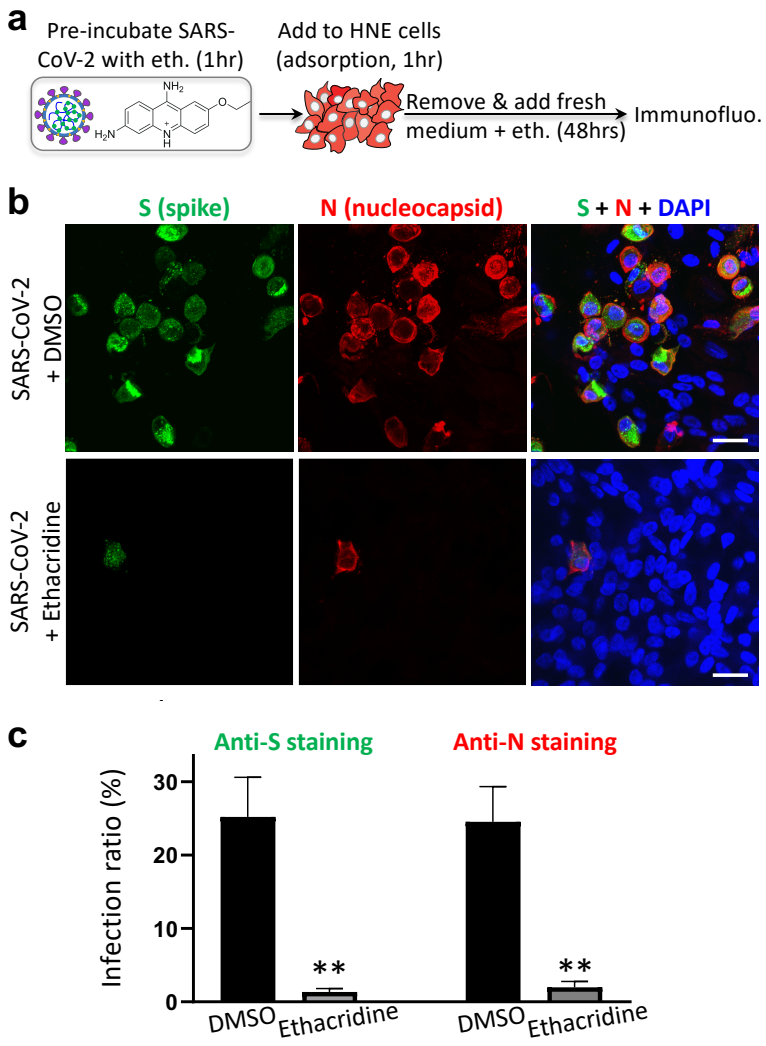

Fig. 5. Ethacridine blocks SARS-CoV-2 in primary human nasal epithelial cells. (**a**) Schematic showing the experimental design, see methods for details. (**b**) Representative images of immunostaining against spike (S) and nucleocapsid protein (N) in HNE cells 48 hours after viral infection in the presence ethacridine (5 μM) or DMSO (control), or no infection (mock). (**c**) Quantification of infection ratio based on anti-S or anti-N staining. Data are mean $\pm$ SEM (three biological replicates). **: p value < 0.01. Scale bar, 20 μm.

265 The current work started with developing a target-specific cell-based screening
266 assay. We developed the Mpro sensor, and our screen of 1622 FDA-approved drugs led
267 to identification of nine drugs that inhibit Mpro activity and show anti-SARS-CoV-2
268 activity. We characterized the antiviral property of five drugs further. Four of them,
269 including simeprevir, ABT-199, hydroxyprogesterone and cinacalcet effectively inhibited
270 Mpro and blocked SARS-CoV-2. This suggests that these four drugs inhibit SARS-CoV-
271 2 mainly by inhibiting Mpro activity. These drugs have similar or better EC50 than
272 ebselen, and thus they may be repurposed as potential therapies against COVID-19.
273 Furthermore, previous computational docking predicted that simeprevir and venetoclax
274 (ABT-199) bind and inhibit Mpro [18,19]. Hydroxyprogesterone inhibits SARS-CoV-2, but
275 its mode of action is unclear [20]. Our data suggests that hydroxyprogesterone may block
276 SARS-CoV-2 by inhibiting Mpro activity. Thus, our FlipGFP-based HTS approach
277 enable screening Mpro inhibitors in the cellular context, can be expanded to visualize
278 activity of key proteases of other viruses at BSL2 and to identify their inhibitors.
279 The most potent antiviral drug discovered in current work, ethacridine, showed
280 stronger antiviral potency than remdesivir and very little cell toxicity (**Fig. 3e**). It blocks
281 SARS-CoV-2 mainly by inactivating the viral particles. First, unlike the other identified
282 drugs that show similar range of IC_{50} in inhibiting Mpro and EC50 against SARS-CoV-2,
283 ethacridine has much higher anti-viral potency (EC_{50} ~ 0.08 μM) than its Mpro-inhibiting
284 activity (IC_{50} ~ 3.5 μM). This indicates that ethacridine's main mode of action is not via
285 inhibiting Mpro. Second, we provide direct evidence that after ethacridine treatment,
286 SARS-CoV-2 particles lose their infectivity and cannot infect or bind host cells. On the
287 other hand, ethacridine does not block viral RNA replication as shown by the qRT-PCR
288 data. Therefore, our data suggest that ethacridine blocks SARS-CoV-2 mainly by
289 inactivating the viral particles with no effect on viral RNA replication. The detailed
290 mechanisms of how ethacridine inactivates the viral particles will require further
291 investigation, such as potential ultrastructural changes of viral particles and binding of
292 ethacridine to viral RNA and/or protein.
293 Our findings reveal a new approach against SARS-CoV-2 via inactivating viral
294 particles, of which the efficacy is expected to be cell type-independent. Indeed,
295 ethacridine blocks SARS-CoV-2 in human cell line $A549^{ACE2}$ cells and also in primary
296 HNE cells. Furthermore, ethacridine is not toxic in various animal models including rat,
297 mice and rabbits. For example, mice treated with 20 mg/kg ethacridine by i.p. injection
298 showed no toxicity [21]. While currently ethacridine is mainly used as a topical wound
299 disinfectant, it has been applied to patients for treating puerperal sepsis via intravenous
300 injection [22]. Thus, it is plausible to validate its antiviral effect in animal models and
301 COVID-19 patients. Moreover, because it blocks the coronavirus by directly inactivates
302 the viral particles, ethacridine may be complemented with other pathway-targeted drugs
303 such as the replicase inhibitor remdesivir in treating COVID-19 patients for a better
304 clinical outcome.
305

306 **Methods**
307
308 **Plasmid construction**
309 Plasmid constructs were created by standard molecular biology techniques and confirmed
310 by exhaustively sequencing the cloned fragments. To create pcDNA3-Mpro-flipGFP-
311 T2A-mCherry, the GFP10-E5-GFP11-Mprosubstrate-K5 fragment was first generated by
312 PCR with an overlapping primer with coding sequence of the MPro substrate,
313 AVLQSGFR. This fragment was then digested with NheI and AflII and inserted into the
314 pcDNA3-TEV-flipGFP-T2A-mCherry [11].
315
316 **Characterization of GFP-based Mpro activity sensor FlipGFP^{Mpro}**
317 To check the FlipGFP^{Mpro} signal in the presence of wildtype or mutant MPro of SARS-
318 CoV-2, HEK293T cells were seeded onto eight-well plate and 24 hours later, 40 ng of
319 pcDNA3-FlipGFP^{Mpro}-T2A-mCherry was transfected with 40 ng of pLVX-EF1alpha-
320 nCoV2019-nsp5-2xStrep-IRES-Puro (expressing wildtype Mpro of SARS-CoV-2) or
321 pLVX-EF1alpha-nCoV2019-nsp5-C145A-2xStrep-IRES-Puro (expressing C145A MPro
322 mutant). To check the FlipGFP^{Mpro} signal after SARS-CoV-2 infection, HEK293T on 10-
323 mm coverglasses were transfected with 200 ng of pcDNA3.1-hACE2 (Addgene,
324 #145033) 24 hours later. Those 293T cells were further infected with SARS-CoV-2 at an
325 MOI of 0.5. At 24 hours after infection, 293T cells were fixed and processed for
326 immunostaining against dsRNA (Scicons, 10010500) and visualized with goat anti-
327 mouse IgG H&L (Cy5 ®) (Abcam, ab6563). Images were taken using Nikon Eclipse Ti-
328 E Spinning Disk under 20X and 60X. The cell pixel intensity in the GFP and mCherry
329 channels were scored using Analyze Particle function in ImageJ. The ratio of GFP pixel
330 intensity against mCherry pixel intensity was then compared in cells with wildtype and
331 mutant MPro or in cells with SARS-CoV-2 or mock infection.
332
333 **High-throughput screen (HTS) against the FDA-approved library**
334 An FDA-approved drug library (MedChemExpress) containing 1622 compounds was
335 used for HTS. For initial screening, 293T cells were seeded onto a 96-well plate,
336 incubated overnight and transfected with 20 ng of pcDNA3-Mpro-flipGFP-T2A-mCherry
337 and 20ng pLVX-EF1alpha-nCoV2019-nsp5-2xStrep-IRES-Puro encoding MPro using
338 calcium-phosphate transfection. At 3 hours after transfection, compounds were added to
339 individual wells at a 100X dilution for a final concentration of 20 μM. Verification of the
340 120 hits from the initial screening and further IC_{50} testing of the 12 hits followed a
341 similar protocol except that a decreasing concentration series was used. Images were
342 acquired 20 hours after transfection in the GFP and mCherry channels with a Nikon
343 Eclipse Ti-E Spinning Disk. The cells' pixel intensity in the GFP and mCherry channels
344 were scored using Analyze Particle function in imageJ. MPro activity was calculated as
345 the ratio of the GFP pixel intensity versus the mCherry pixel intensity.
346
347 **Antiviral assay**
348 The African green monkey kidney Vero E6 cell line was obtained from the American
349 Type Culture Collection (ATCC, no. 1586) and maintained in Minimum Essential
350 Medium (MEM; Gibco Invitrogen) supplemented with 10% fetal bovine serum (FBS;
351 Gibco Invitrogen), 1% penicillin-streptomycin-glutamine (Gibco Invitrogen), at 37°C in a

352 humidified 5% CO_2 incubator. A clinical isolate of SARS-CoV-2 (USA-WA1/2020, BEI
353 Cat No: NR-52281) was propagated in Vero E6 cells. Viral titers were quantified with a
354 plaque assay. All the infections were performed at biosafety level-3 (BSL-3).
355 To assess the antiviral activity, ~70% confluent monolayers of Vero E6 cells
356 (3×10^5 cells/well in 24-well plates) were pretreated with drugs at different concentration
357 for 3 hours (pretreatment) and then infected with SARS-CoV-2 (MOI=0.5) at 37ºC for 1
358 hour. The virus solution was removed, cells were further cultured with fresh medium
359 containing drugs at different concentrations. At 16 hours post-infection, viral titers of the
360 supernatants were detected with a plaque assay.
361
362 **Plaque assay**
363 Confluent monolayers of Vero E6 cells grown in six-well plates were incubated with the
364 serial dilutions of virus samples (250 µl/well) at 37ºC for 1 hour. Next, the cells were
365 overlayed with 1% agarose (Invitrogen) prepared with MEM supplemented with 2%
366 FBS. Three days later, cells were fixed with 4% formaldehyde for 2 hours, the overlay
367 was discarded, and samples were stained with crystal violet dye.
368
369 **Viral RNA quantification**
370 Viral RNA (vRNA) was extracted from cell pellets or supernatants with Tri-reagent
371 (Ambion), following the manufacturer's instructions. The supernatant samples were
372 pretreated with RNAse A for 2 hours at 37ºC to remove non-encapsidated RNA. These
373 samples were also spiked with equivalent volumes of *Drosophila* C Virus (DCV) to
374 enable normalization, based on variation in RNA extractions. RNA from supernatants
375 was used directly to make cDNA using the iScript RT Supermix (BioRad). For cell
376 pellets, 1–2 mg of RNA was treated with DNAse I (NEB), x µL and 2 µL of this reaction
377 was used to make cDNA. qPCR was done using the Luna Universal qPCR Master Mix
378 (NEB) and run on a CFX connect qPCR Detection System (BioRad). To determine the
379 number of vRNA copies per ml, plasmids containing the nucleocapsid gene of SARS-
380 CoV-2 (cloned from the USA-WA1/2020 isolate) or the DCV full genome were used as
381 standards and diluted serially 10-fold to determine target copy numbers. Threshold cycle
382 (Ct) values were plotted against the number of target-copies, and the resultant standard
383 curve was used to determine the number of genome equivalents of vRNA in the samples.
384 For cell pellet samples, the vRNA copy number was normalized to the housekeeping
385 gene *huel,* and supernatant samples were normalized to spiked DCV RNA. All samples
386 were within the range of linearity of a standard curve and primers efficiencies were 100%
387 +/- 5%. The primers used for SARS-CoV-2 are 5′-TCCTGGTGATTCTTCTTCAGG-3′
388 and 5′-TCTGAGAGAGGGTCAAGTGC-3′, DCV 5-CAGCAAAGAAACAGCGTGAG-
389 3' and 5′-CACTTGCGCAACAATACGAG-3′, huel 5′-
390 TCAGACGACGAAGTCCCCATGAAG-3′ and 5′-
391 TCCTTACGCAATTTTTTCTCTCTGGC-3′
392
393 **Cytotoxicity assay**
394 Cytotoxicity of the identified drugs on Vero E6 cell was determined with WST-1 cell
395 proliferation assays (ROCHE, 5015944001). Twenty thousand cells were seeded into a
396 96-well plate and incubated for 20–24 h at 37 °C, and 1 µL of each compound at
397 decreasing concentrations was added. After 18 hrs incubation at 37 °C, WST-1 assays

398 were performed according to manufacturer's protocols. All experiments were performed
399 in triplicate.
400
401 **Adsorption assay**
402 The virus sample was supplemented with 5 μM ethacridine or with DMSO and incubated
403 for 1 hour at 37ºC. Samples were added to ~70% Vero E6 cells monolayers on coverslips
404 with an MOI of 100. The cells were immediately placed on ice for 1 hour, and then the
405 virus suspension was quickly removed, and cells were washed three times with ice-cold
406 PBS. Cells were immediately fixed with 4% PFA for 30 min at room temperature. PFA
407 was further washed with PBS and quenched with 1 M glycine in PBS. Immunostaining
408 was further carried out using an antibody against nucleocapsid (Genetex, SARS-CoV-2
409 (COVID-19) nucleocapsid antibody, GTX135357) or an antibody against spike (Genetex,
410 SARS-CoV-2 (COVID-19) spike antibody [1A9], GTX632604) and visualized with goat
411 anti-rabbit IgG H&L (Alexa Fluor® 488) (Abcam, ab150077) or goat anti-mouse IgG
412 H&L (Alexa Fluor® 555) (Abcam, ab150114). Images were acquired using Nikon
413 Eclipse Ti-E Spinning Disk under 60X and processed in ImageJ. Fluorescence signals
414 were calculated by pixel intensity using Analyze Particle function in Image J.
415
416 **Statistics**
417 All statistics were performed in GraphPad Prism. IC_{50} or EC_{50} of MPro inhibition,
418 cytotoxicity and antiviral activity was calculated using the non-linear fit function
419 (Variable slope). Non-paired t-test was used to compare differences between groups. One
420 way-ANOVA and Dunnett's multiple comparisons test was used to compare differences
421 among multiple groups.
422
423 **Acknowledgments:** We thank David Gordon and Nevan Krogan for sharing the cDNA
424 of Mpro of SARS-CoV-2.
425
426 **Funding:** This work was supported in part by NIH (R35 GM131766) to X.S., NIH (R01
427 AI36178, AI40085, P01 AI091575), the Bill and Melinda Gates Foundation and the
428 DARPA Intercept program (Contract No. HR0011-17-2-0027) to R.A.
429
430 **Author contributions:** X.L., X.S. initiated the project and designed the fluorescent
431 assays. X.L., J.Y. prepared the drug library. X.L. performed screening and characterized
432 dose response of Mpro inhibition. P.L., Y.X., R.A. designed the antiviral activity assays.
433 P.L., Y.X. conducted plaque assay. P.L., Y.X., X.L. performed quantitative analysis.
434 M.K. performed RT-qPCR. X. L. performed toxicity assays. P.L., Y.X., X.L. performed
435 and analyzed immuno-staining. P.L., Y.X., T.N., J.V.N., C.W. P. K. J. and R.A. designed
436 the HNE cell infection experiments. P.L. and Y.X. performed viral infection, C.W., T.N.
437 performed cell culturing, C.W. conducted immunostaining and imaging, X.L. performed
438 quantitative analysis of the HNE cells. X.S. wrote initial manuscript, X.L., P.L., Y.X.,
439 M.K., C.W. wrote the methods. All authors edited and contributed to the final draft.
440
441
442 **Competing interests:**
443 X.L., P.L., Y.X., R.A., X.S. have filed a patent on a new use of the identified compounds.

Data and materials availability: All data are available in the main text or in the supplementary information.

Supplementary Information:

Extended data Figs. 1–6

455 **References**

456 1. Zhou, P. *et al.* A pneumonia outbreak associated with a new coronavirus of
457 probable bat origin. *Nature* 1–20 (2020). doi:10.1038/s41586-020-2012-7
458 2. Andersen, K. G., Rambaut, A., Lipkin, W. I., Holmes, E. C. & Garry, R. F. The
459 proximal origin of SARS-CoV-2. *Nat Med* 1–3 (2020). doi:10.1038/s41591-020-
460 0820-9
461 3. Gorbalenya, A. E. *et al.* The species Severe acute respiratory syndrome- related
462 coronavirus: classifying 2019-nCoV and naming it SARS-CoV-2. *Nature*
463 *Microbiology* 1–9 (2020). doi:10.1038/s41564-020-0695-z
464 4. Liu, C. *et al.* Research and Development on Therapeutic Agents and Vaccines for
465 COVID-19 and Related Human Coronavirus Diseases. *ACS Cent. Sci.*
466 acscentsci.0c00272–17 (2020). doi:10.1021/acscentsci.0c00272
467 5. Gordon, D. E. *et al.* A SARS-CoV-2 protein interaction map reveals targets for
468 drug repurposing. *Nature* 1–13 (2020). doi:10.1038/s41586-020-2286-9
469 6. Yin, W. *et al.* Structural basis for inhibition of the RNA-dependent RNA
470 polymerase from SARS-CoV-2 by remdesivir. *Science* eabc1560–10 (2020).
471 doi:10.1126/science.abc1560
472 7. van Hemert, M. J. *et al.* SARS-Coronavirus Replication/Transcription Complexes
473 Are Membrane-Protected and Need a Host Factor for Activity In Vitro. *PLoS*
474 *Pathog* **4,** e1000054–10 (2008).
475 8. Jin, Z. *et al.* Structure of Mpro from COVID-19 virus and discovery of its
476 inhibitors. *Nature* 1–28 (2020). doi:10.1038/s41586-020-2223-y
477 9. Zhang, L. *et al.* Crystal structure of SARS-CoV-2 main protease provides a basis
478 for design of improved α-ketoamide inhibitors. *Science* **368,** 409–412 (2020).
479 10. Dai, W. *et al.* Structure-based design of antiviral drug candidates targeting the
480 SARS-CoV-2 main protease. *Science* eabb4489–10 (2020).
481 doi:10.1126/science.abb4489
482 11. Zhang, Q. *et al.* Designing a Green Fluorogenic Protease Reporter by Flipping a
483 Beta Strand of GFP for Imaging Apoptosis in Animals. *J Am Chem Soc* **141,**
484 4526–4530 (2019).
485 12. Tsien, R. Y. The green fluorescent protein. *Annu Rev Biochem* **67,** 509–544
486 (1998).
487 13. Szymczak, A. L. *et al.* Correction of multi-gene deficiency in vivo using a single
488 'self-cleaving' 2A peptide-based retroviral vector. *Nat Biotechnol* **22,** 589–594
489 (2004).
490 14. Zhang, J., Chung, T. & Oldenburg, K. A Simple Statistical Parameter for Use in
491 Evaluation and Validation of High Throughput Screening Assays. *Journal of*
492 *Biomolecular Screening* **4,** 67–73 (1999).
493 15. Lo, H. S. *et al.* Simeprevir suppresses SARS-CoV-2 replication and synergizes
494 with remdesivir. *bioRxiv* **395,** 1054–20 (2020).
495 16. MD, Y. W. *et al.* Remdesivir in adults with severe COVID-19: a randomised,
496 double-blind, placebo-controlled, multicentre trial. *The Lancet* **395,** 1569–1578
497 (2020).
498 17. WHO Solidarity trial consortium *et al.* Repurposed antiviral drugs for COVID-19
499 –interim WHO SOLIDARITY trial results. *medRxiv* **17,** e1003252–17 (2020).

500 18. Hosseini, F. S. & Amanlou, M. Anti-HCV and anti-malaria agent, potential
501 candidates to repurpose for coronavirus infection_ Virtual screening, molecular
502 docking, and molecular dynamics simulation study. *Life Sci.* **258,** 118205 (2020).
503 19. Chen, Y. W., Yiu, C.-P. B. & Wong, K.-Y. Prediction of the SARS-CoV-2 (2019-
504 nCoV) 3C-like protease (3CLpro) structure: virtual screening reveals velpatasvir,
505 ledipasvir, and other drug repurposing candidates. *F1000Res* **9,** 129–18 (2020).
506 20. Jeon, S. *et al.* Identification of Antiviral Drug Candidates against SARS-CoV-2
507 from FDA-Approved Drugs. *Antimicrobial Agents and Chemotherapy* **64,** 270–9
508 (2020).
509 21. Rotin, L. E. *et al.* Ibrutinib synergizes with poly(ADP-ribose) glycohydrolase
510 inhibitors to induce cell death in AML cells via a BTK-independent mechanism.
511 *Oncotarget* **7,** 2765–2779 (2016).
512 22. Oginz, P. & (null). Intravenous injections of rivanol in puerperal sepsis. *AJS* 647–
513 650 (1929). doi:10.1016/S0002-9610(29)90444-X
514

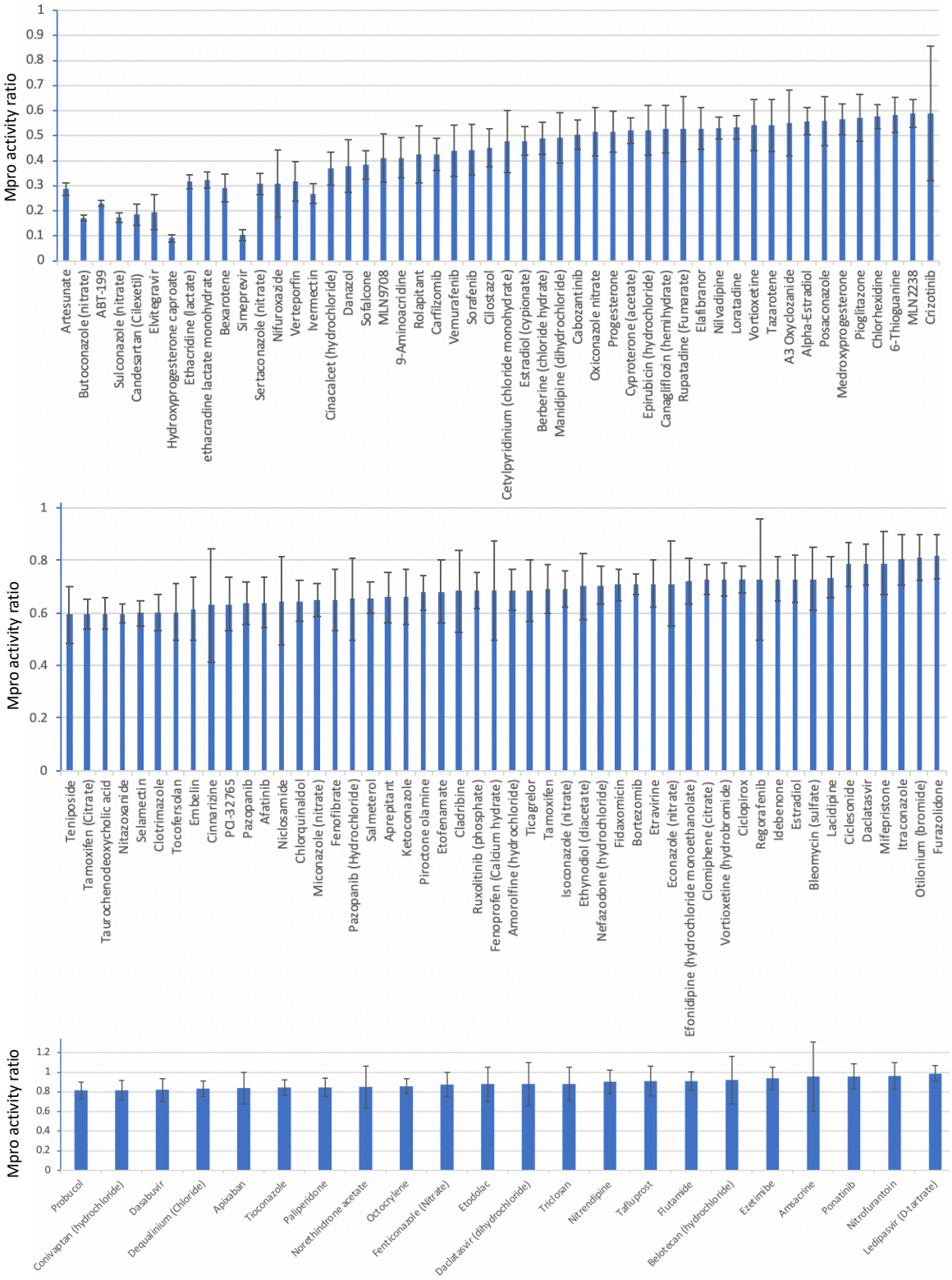

Extended data Fig. 1. Verification of the selected top 120 drugs using the Mpro activity reporter FlipGFP^{Mpro}. Ratio of Mpro activity was calculated based on FlipGFP^{Mpro} fluorescence of drug-incubated HEK293 cells, divided by that of DMSO-treated HEK293 cells. FlipGFP^{Mpro} fluorescence was normalized by mCherry in HEK293 cells, which co-expressed FlipGFP^{Mpro}, mCherry, and Mpro**.** Data are mean $\pm$ SD (n = 5).

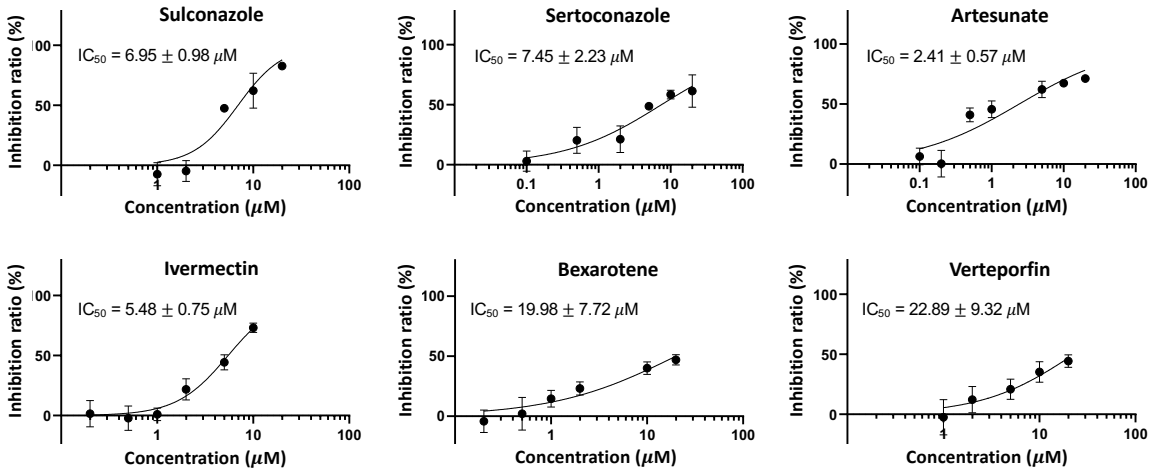

Extended data Fig. 2. Dose-response curve of Mpro inhibition. The Mpro activity was determined as FlipGFP fluorescence normalized by mCherry. The ratios of Mpro activity were calculated by normalizing Mpro activity with that of cells treated with DMSO. Inhibition ratio was calculated as (1-(ratio of Mpro activity)) X100%. Data are mean ± SD (n = 5). IC_{50} was represented as mean ± SEM (n = 5).

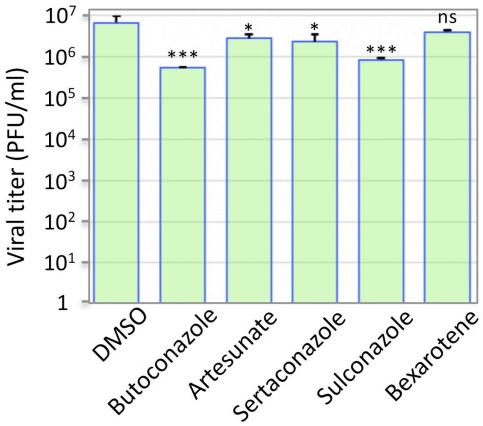

Extended data Fig. 3. Antiviral activities of the identified drugs. Antiviral activities of five drugs (5 μM) were quantified by a plaque assay with SARS-CoV-2 in Vero E6 cells. Data are mean $\pm$ SD (n = 3). *: p value < 0.05; ***: p value < 0.001. ns: not significant. PFU: plaque-forming unit.

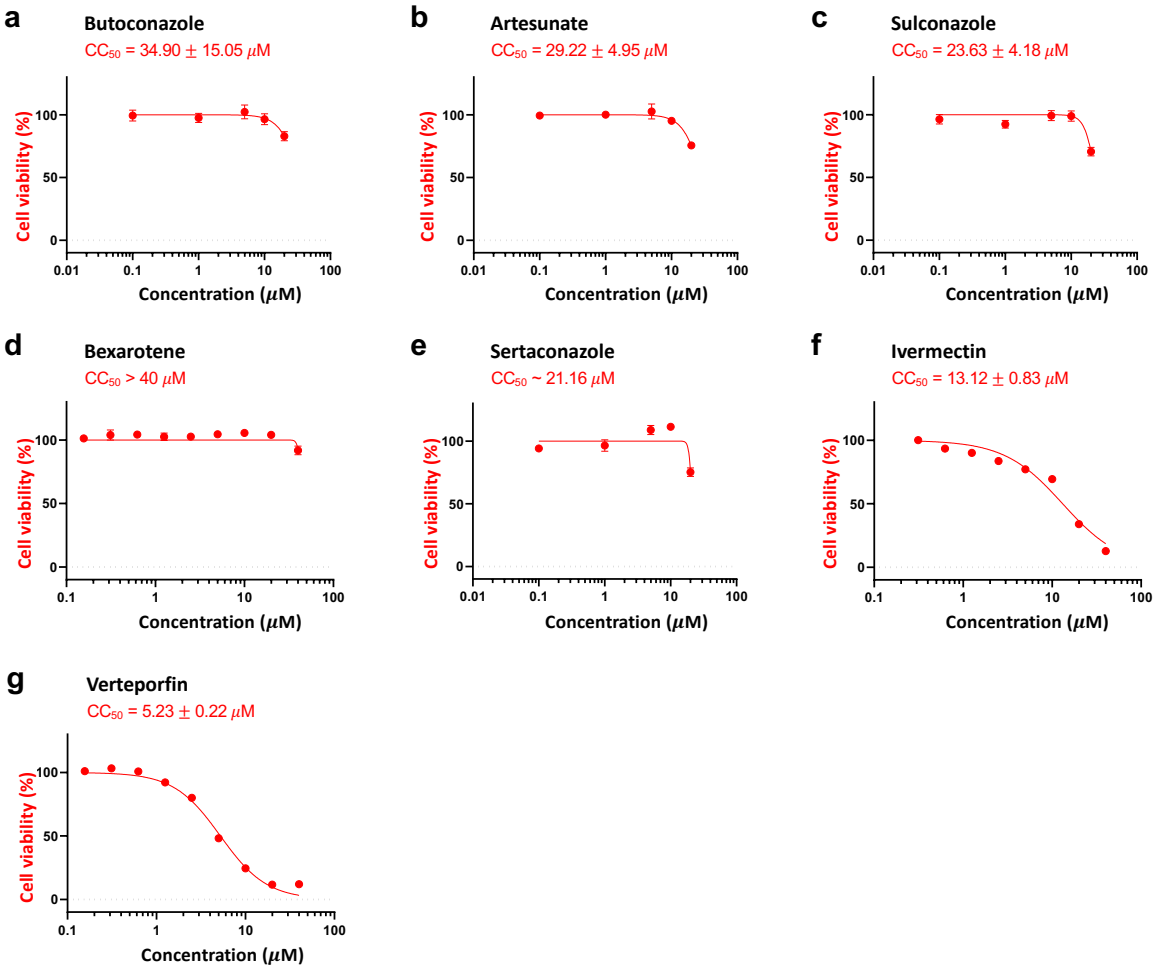

Extended data Fig. 4. Cytotoxicity of the identified drugs. The cytotoxicities of the indicated compounds were determined in Vero E6 cells with the WST-1 assay. CC_{50} is represented as mean ± SEM (n = 3).

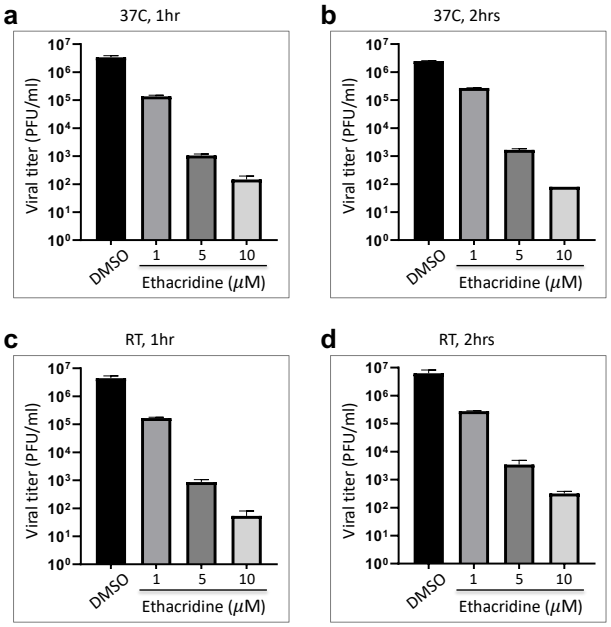

Extended data Fig. 5. Virucide effect of ethacridine on SARS-CoV-2. Effects of ethacridine on the infectivity of SARS-CoV-2 were examined using plaque assay at 37ºC (**a**, **b**) or in the room temperature (RT) (**c**, **d**). SARS-CoV-2 was mixed with ethacridine for 1 or 2 hours before being added to infect Vero E6 cells. Data are mean ± SEM (n = 3).

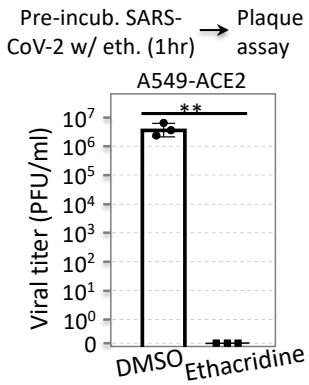

Extended data Fig. 6. Quantitative analysis of viral titer by plaque assay in the human cells A549 that stably express ACE2. SARS-CoV-2 was pre-incubated with ethacridine (5 uM) for 1hr, followed by plaque assay on the human A549 cells stably expressing human ACE2 ($A549^{ACE2}$).